

Research Article

Parametric Study on Dynamic Response of FRP Masonry Structures under the Impacts of Debris Flow

Peizhen Li ^{1,2}, Tangzhenhao Li,² Zheng Lu ^{1,2} and Jin Li²

¹State Key Laboratory of Disaster Reduction in Civil Engineering, Tongji University, Shanghai, China

²Research Institute of Structural Engineering and Disaster Reduction, Tongji University, Shanghai, China

Correspondence should be addressed to Zheng Lu; luzheng111@tongji.edu.cn

Received 10 July 2017; Accepted 8 January 2018; Published 8 February 2018

Academic Editor: Naveed Ahmad

Copyright © 2018 Peizhen Li et al. This is an open access article distributed under the Creative Commons Attribution License, which permits unrestricted use, distribution, and reproduction in any medium, provided the original work is properly cited.

The aim of this study was to investigate the influences of different parameters on the performance of fiber reinforced polymer (FRP) masonry structures under debris flow using finite element models that were established using the software LS-DYNA. The overall structural responses under the impacts of viscous debris flows were analyzed based on an in-depth parametric study of some key factors (fiber types, relative impact positions, etc.). The results show that the diagonal and intersecting parallel types of FRP arrangements elicit better performances than horizontal types. Use of wider fiber cloths leads to the minimization of the structural response after its impact by debris flow. In addition, glass fiber reinforced polymer (GFRP) yields the best results among all studied materials in reducing local damage, while carbon fiber reinforced polymer (CFRP) yields a better overall structural response. Impact positions at the center of the wall are more unfavorable than those at the corners.

1. Introduction

Debris flow, usually caused by blizzards or heavy rains, is a solid-liquid, two-phase fluid, containing a large number of sand and gravel particles [1]. Mountain areas, where debris flow is generated from frequent eruptions [2], account for two-thirds of China's land area [3]. In these areas, masonry structures constitute one of the main structural forms used in inhabited areas. According to published statistical data, masonry bricks are used to occupy 70% of construction materials in China. Besides, 80% of houses in mountainous areas have been built using bricks [4]. However, the resistance of such masonry structures to geological disasters is generally quite weak, and these parts of China have not been well developed economically [5]. Thus, debris flow has posed a great threat to the economic development and personnel safety in mountain areas. As a line of defense against debris flow, structures play an important role in ensuring the safety of residents' lives and their properties. Additionally, according to the "National Comprehensive Disaster Prevention and Reduction Plan" promoted by the Chinese government, disaster prevention and reduction is one of the most important

national strategies [6]. Consequently, taking effective measures to strengthen the structures in areas threatened by debris flow is of significant importance.

In order to decrease losses caused by debris flow, many scholars all over the world have been expending efforts to study debris flow, as well as propose various reinforcing methods, for example, energy dissipation methods [7–14]. Wu [15] used a cantilever beam, or a simply supported beam, to simulate the dam and other structures and obtained an equation of impact force based on material mechanics. This method assumed that rocks and structures were elastic and ignored the plastic deformation which might have occurred under debris impact. Accordingly, this assumption resulted in an overestimation of the impact force of rocks. Based on such studies, scholars began to consider viscoelastic and elastoplastic behaviors of the material during collisions and developed other formulations and equations [16]. The contact stiffness method was based on a spring-mass system in which an effective contact stiffness was needed. This method was recommended in the Highway Bridge Design Specification published by the National Association of Australian State Road Authorities [17]. Some scholars established calculation

methods on the debris flow force under rock impacts from the viewpoint of energy conversion. Hungr [18] analyzed the relationship between the impact energy of debris flow and the bending deformation energy of a beam, by simplifying the representation of the support scheme to a cantilever scheme. In addition, he introduced a structural stiffness coefficient and proposed a practical calculation formula for the debris flow force.

In regard to the reinforcing method, FRP plays an important role in repairing and reinforcing building structures because of its high strength, light weight, convenience in construction, and abilities of corrosion and aging resistance [19]. In a seismic test, the load-bearing capacity of a brick wall, reinforced by carbon fiber reinforced polymer (CFRP), was significantly improved in the elastic stage [20]. Seible [21] proved that the ductility of a brick wall reinforced by CFRP can be improved under earthquake actions. Based on the experiment of damaged masonry walls strengthened by CFRP under low-cyclic reversal tests, Wang [22] proved that the function of CFRP was similar to that of the rod in the truss model. CFRP delayed or prevented the development of cracks and improved the dynamic response of masonry walls.

Based on these studies, it can be concluded that FRP reinforcement can effectively increase the structural stiffness to resist seismic loads. However, the performances of conventional and FRP-reinforced structures under debris flow impact have been rarely investigated [23]. In fact, in poor mountainous area, there are plenty of masonry structures which are vulnerable to debris flow loads [24]. According to the study of Guo et al. [25], FRP is favorable for masonry walls for its impact resistance. Hence, this FRP strengthening method may constitute a cost-effective way to increase the structural resistance to debris flow. However, such a reinforcement method cannot be applied in construction without determining its parameters since they are key factors in influencing the structural performance. Consequently, this study mainly focuses on the dynamic response of FRP-reinforced masonry structures under debris flow impacts, based on an extensive parametric study of some of key factors, including fiber reinforcement arrangement, width and types of the FRP material, and relative impact positions. Simulations are developed herein in accordance with the following steps. (1) Select proper material models and element types based on relevant research experience. (2) Establish structural models. To complete this study, thirteen two-story models are established based on four assumptions. (3) Analyze structural response under dead load by dynamic relaxation method. This is a necessary step to consider the influence of the dead load and the slurry load. (4) Investigate failure process. The parametric study is developed mainly at this step by focusing on the rock impact time history curves, damage of the wall, and the displacement of the structure.

2. Numerical Stimulation

2.1. Debris Flow Model. The impact of large rocks in debris flow is the main cause of structural damage [26]. The most popular method used to calculate the impact force of rocks in debris flow is the quasi-static method. However, this method

does not take into account the time effect and complex contacts. By using the LS-DYNA software, these defects can be solved [27]. LS-DYNA is a general-purpose, finite element program, which is suitable for solving nonlinear collision problems. The modeled and calculated numerical results have been shown to be in good agreement [28–30]. Wei [31] simulated clay brick unreinforced masonry walls through the use of LS-DYNA software. It is pointed out that the numerical model can reasonably predict the damage levels by comparing them with field test data. According to Elsanadedy [32], FRP can be well-simulated through LS-DYNA by studying reinforced concrete one-way slabs upgraded with FRP composites.

Impact position and velocity are two core parameters of the rock in debris flow. According to Proske [33], the largest impact force of debris flow concentrates in regions corresponding to the range of 20–33% of flow depths. He [34] found that rocks concentrated at 1/2 of the maximum depth are more unfavorable to debris flow. Based on Zeng's study [35], the typical velocity of boulders in debris flow ranges between 3.5 m/s and 5 m/s. Based on these studies, it is assumed herein that the velocity of the rock is 5 m/s, and the impact position—whose depth is equal to the height of the first floor of the structure—is at 1/2 of the depth of the debris flow. The density is selected as 2000 kg/m³. Furthermore, the rock's size is 0.5 m × 0.5 m × 0.5 m, and its density is defined as 2800 kg/m³, resulting in the total mass of approximately 350 kg.

2.2. Masonry Structural Model. The masonry structural model comprises a typical two-story masonry structure designed based on Chinese codes [36] and consists of clay bricks with a thickness of 240 mm. The story height is 3.3 m and the layouts are shown in Figure 1. The compressive strengths of mortar and brick are 7.5 MPa and 15.0 MPa, respectively. The FRP is arranged at the wall of axis ③, and every piece of FRP comprises only one layer.

For FRP structures, including the column, ring beam, and masonry wall, the minimum element mesh size was 0.03 m, and the maximum element mesh size was 0.12 m. For slab and the roof, the element mesh size was 0.12 m. In addition, for steel, the minimum element mesh size was 0.1 m, and the maximum element mesh size was 0.2 m. Full 3D finite element model with the boundary conditions is shown in Figure 2. All freedom of the bottom nodes of the model is constrained.

The construction of the masonry model was based on the following assumptions.

(a) FRP behaves as an elastic material during the impact. (b) The masonry walls and FRP share the same nodes in the constructed model [37]. (c) The hydrostatic pressure is ignored in the simulation. (d) The slurry of the debris flow is assumed to behave as a one-dimensional Newtonian fluid, and it impacts the wall perpendicularly.

2.3. Material Model. The anisotropic brittle damage model (MAT96) is selected to simulate masonry materials [38, 39]. This an anisotropic brittle damage model which admits progressive degradation of tensile and shear strengths across

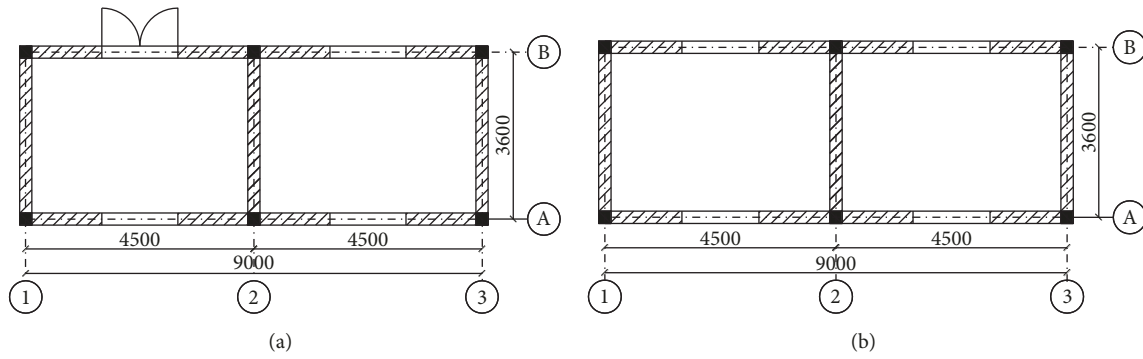


FIGURE 1: Layouts of the model: (a) first floor and (b) second floor.

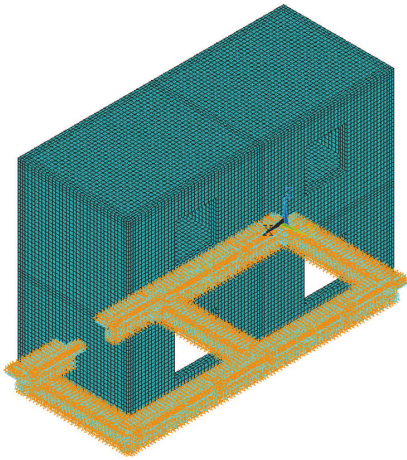


FIGURE 2: Full finite element model.

smear cracks that are initiated under tensile loadings [40]. The continuous surface cap model (CSCM), which considers the hardening, damage, and strain rate effects of the material [41], is used to simulate concrete. According to the results of Xu and Fang [42], carbon fiber has a large elastic modulus, and the tensile properties of this material were not affected by the strain rate. Accordingly, carbon fiber could be treated as an ideal elastomeric material. The constitutive relationship of carbon fiber is modeled by the stress-strain relationship corresponding to a linearly elastic material [43]. Moreover, the stiffness of rock is much larger than that of the structure, and further considerations of this matter are beyond the main focus of this study. Therefore, the rock is assumed to be rigid.

3. Comparative Analyses of Reinforced and Unreinforced Models

Before conducting a parametric study on the dynamic response of FRP-reinforced masonry structures under debris flow, it is necessary to evaluate the effectiveness of the FRP-reinforced masonry structure. Hence, the corresponding comparative analyses of reinforced and unreinforced models are discussed in this section. As it is shown in Figure 3, the

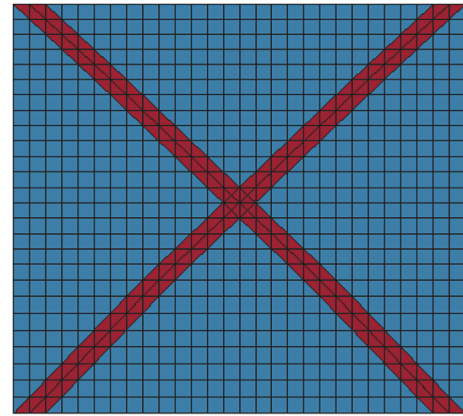


FIGURE 3: Arrangement of FRP.

FRP is arranged in a diagonal arrangement in the reinforced model. The width of FRP of the model is 150 mm, and its thickness is 0.167 mm. The unreinforced model is regarded as the control model. The rock impact occurs at the center of the wall.

3.1. Dynamic Relaxation Analyses. Dynamic relaxation is a numerical method aiming to find a geometry where all forces are in equilibrium. It is a step employed to consider the influences of the dead load and the slurry load before the rock impact.

According to Tang et al.'s study [44], hydrodynamic pressure of the slurry can be calculated using the formula $F = K\rho v^2$. The empirical coefficient K depends on the type and stage of debris flow. ρ is the density of slurry. v is the velocity of slurry. The slurry load can be simplified as uniformly distributed load [39], which is loading on the impacted cross wall. In this article, the slurry load is considered only in stationary stage. Hence, the empirical coefficient equals to 0.5. The parameters of hydrodynamic pressure of the slurry are shown in Table 1.

In simulation process, loading curve was defined by key word *DEFINE-CURVE. Then, the uniformly distributed load was applied on the surface elements of impacted wall

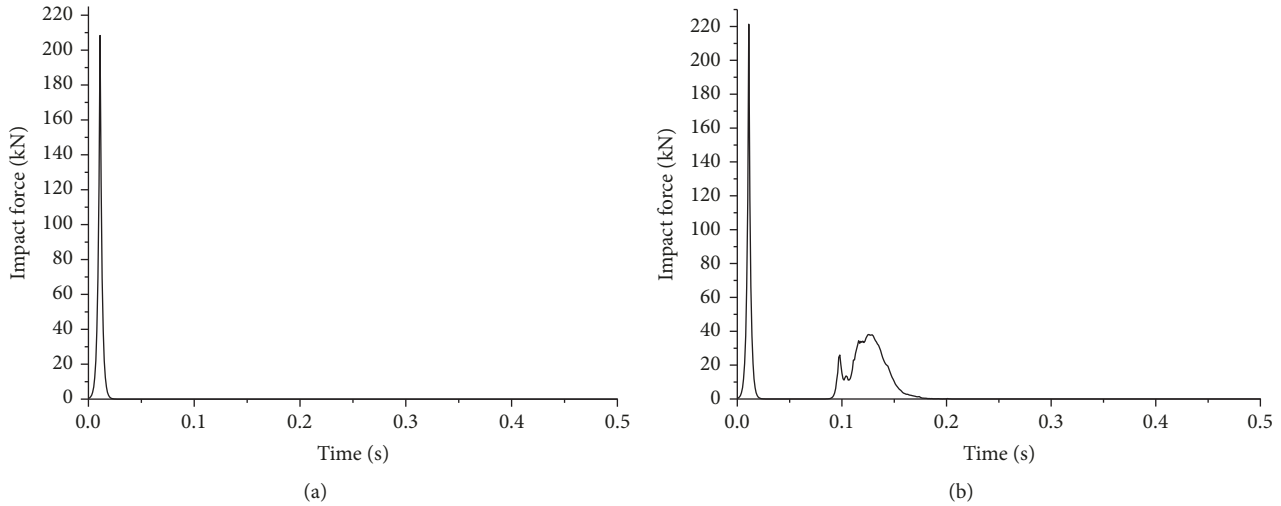


FIGURE 4: Impact force of the two models: (a) control model and (b) reinforced model.

TABLE 1: The parameters of hydrodynamic pressure of the slurry.

Type of debris flow	Density (kg/m^3)	Velocity (m/s)	Stationary stage empirical coefficient
Viscous debris flow	2000	5	0.5

by defining key word *SET-SEGM and *LOAD-SEGMENT-SET. Dynamic relaxation was completed by defining key word *CONTROL_DYNAMIC_RELAXATION.

In this step, the maximum stress of the control model is 1.61 MPa, while the corresponding maximum stress value for the reinforced model is 1.45 MPa. For the entire model, the stress of the reinforced model is relatively smaller. Similar to the stress distribution, the displacement of the reinforced model is smaller than that of the control model. The maximum displacement of the control model is 2.52 mm, while that for the reinforced model is 1.39 mm.

3.2. Rock Impact Time History Curves. After the dynamic relaxation analysis, the rock began to move to the masonry wall at a speed of 5 m/s when $T = 0$ s. As shown in Figure 4, the collision between the rock and the wall triggered the impulsive force.

It can be seen that the impact force reaches its maximum value within 10 ms. The peak forces for the control and reinforced models are 208 kN and 218 kN, respectively. The reason for this finding is that the stiffness of the reinforced model is larger than that of the control model, since the FRP contributes to the increase of the stiffness. Moreover, owing to the impedance of the FRP, there are two successive impulses in the reinforced model. However, a second impact on FRP is favorable since the rest of the structure can be made full use of. In other words, an increased proportion of the energy of the rock is absorbed by the reinforced model. Consequently, the damage in the reinforced house that is expected to be caused by the rock could be reduced. Figure 5 shows the

condition during the impact at $T = 15$ ms. It can be seen that the rock has crashed into the structure in the control model at this moment, while the rock is stopped by the FRP of the reinforced model. This result also indicates that the reinforced model performs better than the unreinforced one.

3.3. Displacement Response. Four typical nodes are selected to analyze the overall displacement response of the structure. The position and number of the nodes are shown in Figure 6. Figure 7 shows the displacement time history curves of these typical nodes. It can be seen that the fluctuation of the displacement of the reinforced model is much smaller than that of the control model. In addition, as it is shown in Table 2, the maximum displacement of the control model is a little larger than that of the reinforced model. This is because FRP absorbs part of the energy of the rock, and because the masonry walls of the reinforced model are fully used.

In summary, the reinforced model performs better than the unreinforced model. Therefore, a parametric study on the dynamic response of FRP-reinforced masonry structures under debris flow impact is necessary.

4. Parametric Study on Dynamic Responses

4.1. Fiber Reinforcement Arrangement

4.1.1. Scheme of Reinforcement. Three finite element models are established. They are reinforced by FRP and classified in three types, namely, the diagonal type, the intersecting parallel type, and the horizontal type. The reinforcement scheme is shown in Table 3, and the corresponding finite element models are shown in Figure 8.

4.1.2. Dynamic Response

(a) Rock Impact Time History Curves. Figure 9 shows the impact time history curves for models 1 to 3. It can be seen that the peak values of the impact forces of models 1 to 3 are

TABLE 2: Maximum displacement (mm) of the control and reinforced models.

Node	Model		
	Control model	Reinforced model	Percentage reduction
1	2.14	2.03	5.1%
2	2.16	2.02	6.5%
3	1.69	1.58	6.5%
4	0.35	0.32	8.6%

TABLE 3: Reinforcement scheme with different FRP arrangements.

Number	Width (mm)	Thickness (mm)	Paste type	Area (m ²)
1	340	0.167	Diagonal type	3.08
2	240	0.167	Intersecting parallel type	3.08
3	240	0.167	Horizontal type	3.08

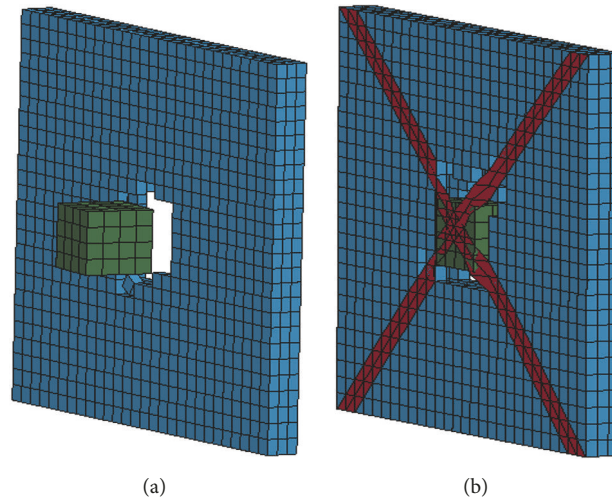


FIGURE 5: The condition of the two models at $T = 15$ ms: (a) control model and (b) reinforced model.

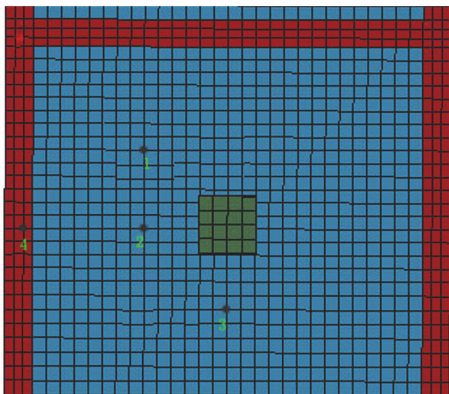


FIGURE 6: Locations of nodes in the impacted transverse wall.

209 kN, 212 kN, and 211 kN, respectively. In addition, based on the irregular pattern of the curves upon rock impact with the FRP, it can be noticed that the impact force is complex. This is because the vibration of the model caused by the

impact triggers the interaction between the rock and the FRP. As it is shown in Figure 9, the arrangement of carbon fiber has influenced the magnitude of the impact force and the duration of the interaction. Among these arrangement types, the horizontal FRP arrangement reduces the force and prolongs the interaction between the rock and the fiber.

(b) *Damage Response.* Figure 10 shows the stress contours for models 1 to 3 at $T = 300$ ms. It can be seen that local damage is the main failure mode. A certain degree of stress concentration occurs at the four corners of the rectangular hole and at the bottom of the wall. Maximum stress appears at the locations of the fixed supports that are connected to the ground. The maximum stress values of models 1 to 3 are 1.06 MPa, 0.94 MPa, and 1.15 MPa, respectively. Based on the stress contours, it can be deduced that the stress values of the diagonal and the intersecting parallel types are smaller, because the stress of the wall distributes more uniformly in these two types. Consequently, these two types of arrangements are more favorable for debris flow resistance. Moreover, it can also be noted that there is variation in

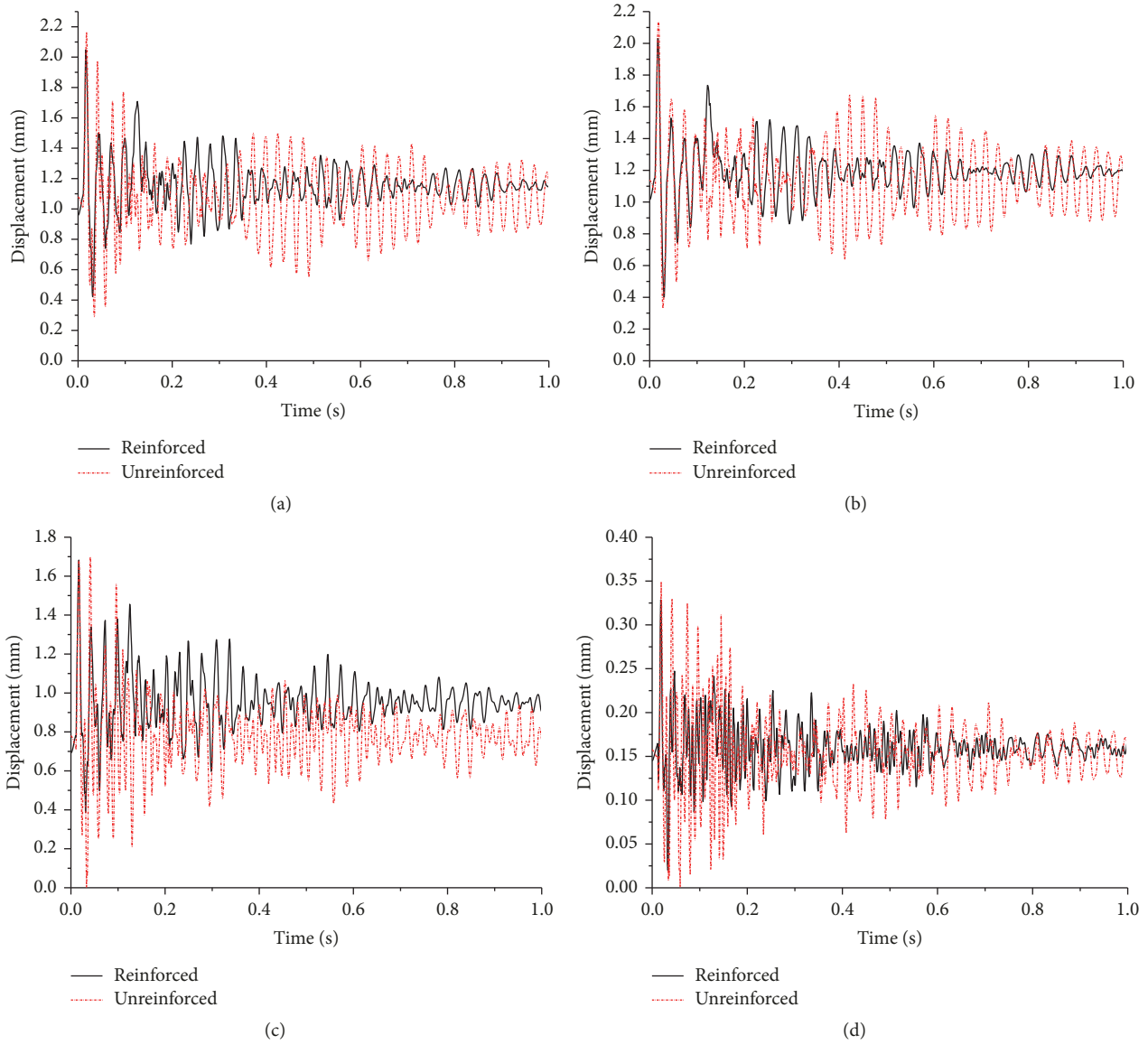


FIGURE 7: Displacement time history curves of nodes: (a) node 1, (b) node 2, (c) node 3, and (d) node 4.

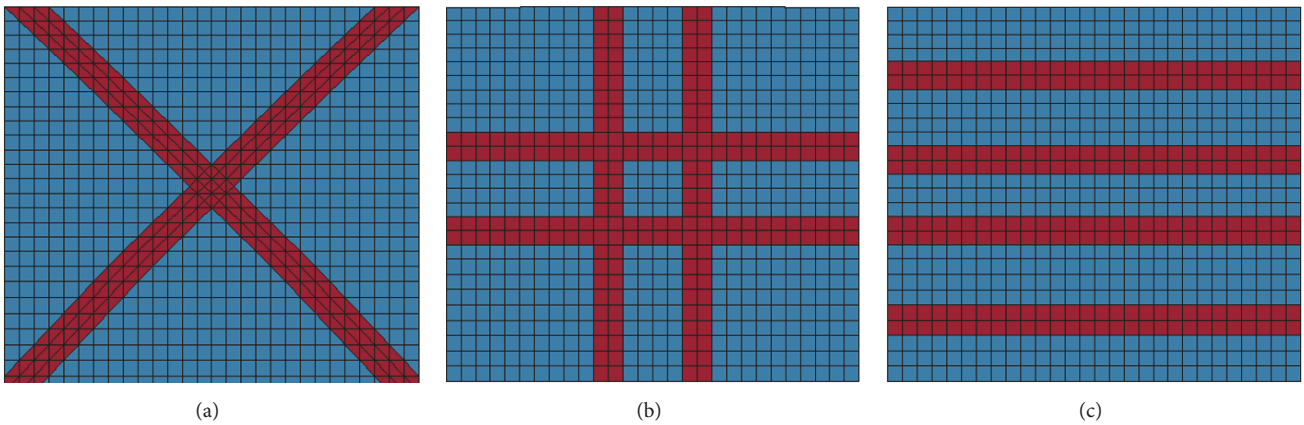


FIGURE 8: Fiber reinforcement arrangements: (a) model 1, (b) model 2, and (c) model 3.

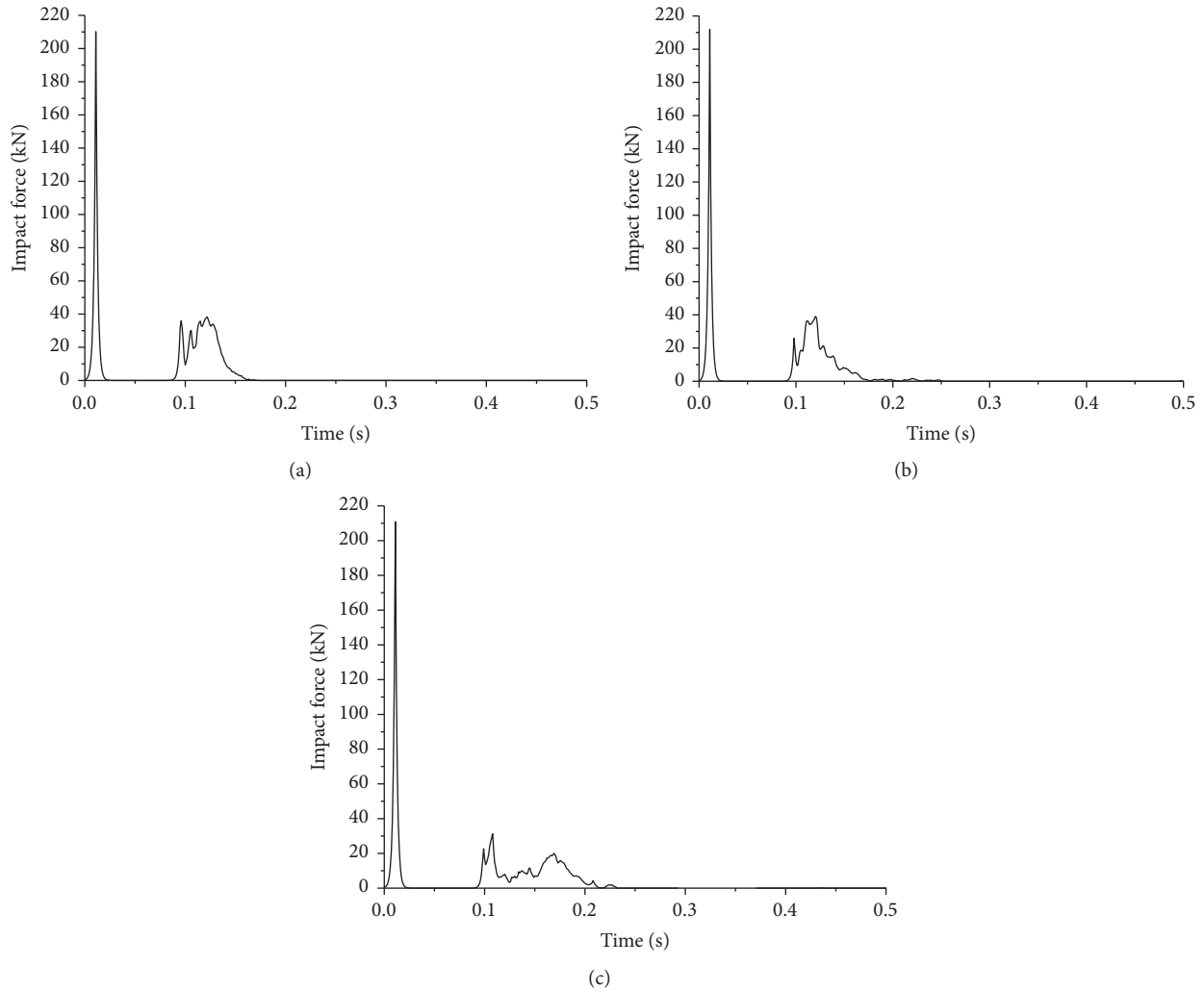


FIGURE 9: Impact time history curves: (a) model 1, (b) model 2, and (c) model 3.

the way local damage develops, in accordance with the arrangement type. It can be seen that the local damage develops along the direction of fiber arrangements. This damage results owing to the change of stiffness, which is affected by FRP. These bricks have a higher stiffness and tend to absorb more energy during the interaction, which results in the local damage.

(c) *Displacement Response.* Four typical nodes are selected to analyze the overall displacement response of the structure. The position and number of the nodes are the same as those shown in Figure 6. Figure 11 shows the displacement time history curves of these typical nodes. It can be seen that the displacement patterns of the nodes in these three models are basically the same. Model 3 yields the largest displacement amplitude, and the largest final residual strain, while model 1 yields the smallest. This is because the arrangement types of models 1 and 2 make the stress distribute uniformly on the wall. In addition, the wave of the time history curve of node 4 is denser than the others, indicating that node 4 has

TABLE 4: Maximum displacements (mm) of models 1 to 3.

Node	Model		
	1	2	3
1	2.00	2.08	2.05
2	2.60	2.54	2.63
3	1.49	1.52	1.56
4	0.23	0.27	0.28

a higher vibration frequency. This is because node 4 is on the structural column, whose out-of-plan stiffness is larger than that of the masonry wall. A higher stiffness leads to a higher vibration frequency.

Table 4 lists the maximum displacement of each typical node. The results from these data are consistent with the elicited results shown in Figure 11. According to these analyses, the diagonal and the intersecting parallel types of FRP arrangements elicit better performances in resisting debris flow than the horizontal type.

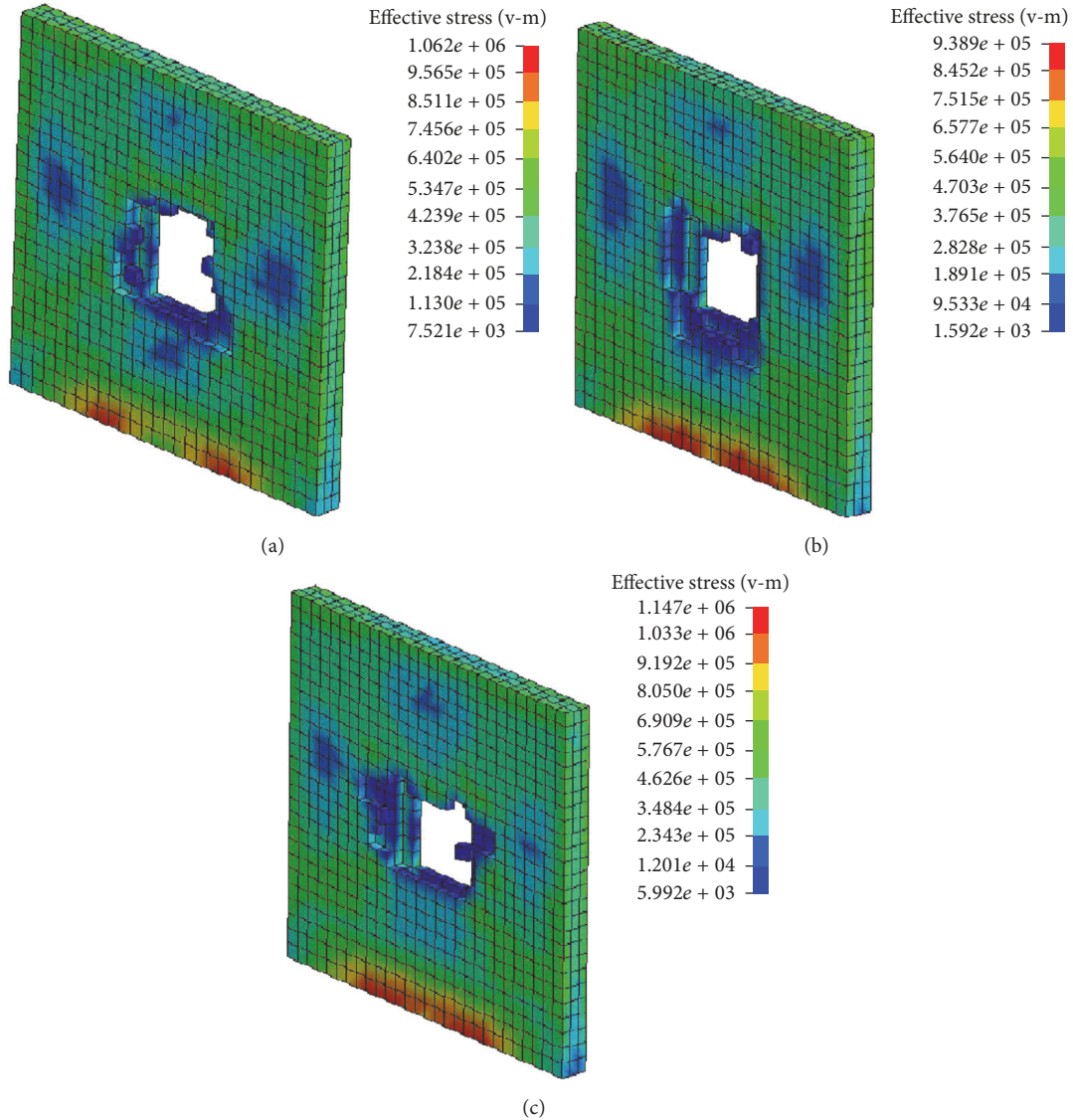


FIGURE 10: Stress contours of impacted walls at $T = 300$ ms: (a) model 1, (b) model 2, and (c) model 3.

TABLE 5: Scheme of reinforcement at different FRP widths.

Number	Width (mm)	Thickness (mm)	Paste type	Area (m ²)
4	150	0.167	Diagonal	1.35
5	250	0.167	Diagonal	2.25
6	250	0.167	Diagonal	3.15

4.2. Fiber Width

4.2.1. Scheme of Reinforcement. Three finite element models are established. The FRP of these models are all arranged in a diagonal arrangement, but with different widths. The scheme of reinforcement is shown in Table 5, and the corresponding finite element models are shown in Figure 12.

4.2.2. Dynamic Response

(a) Rock Impact Time History Curves. Figure 13 shows the impact time history curves from model 4 to model 6. It can be

seen that the peak values of the impact forces of models 4 to 6 are 202 kN, 208 kN, and 209 kN, respectively. The differences of the force values result from the different wall stiffness values, which are affected by the width of the FRP. As it is mentioned in Section 4.1.2, irregular curve patterns result from the vibration of the model.

(b) Damage Response. Figure 14 shows the stress contours for models 4 to 6 at $T = 300$ ms. It can be found that local damage is the main failure mode. A certain degree of stress concentration occurs at the four corners of the hole, and at

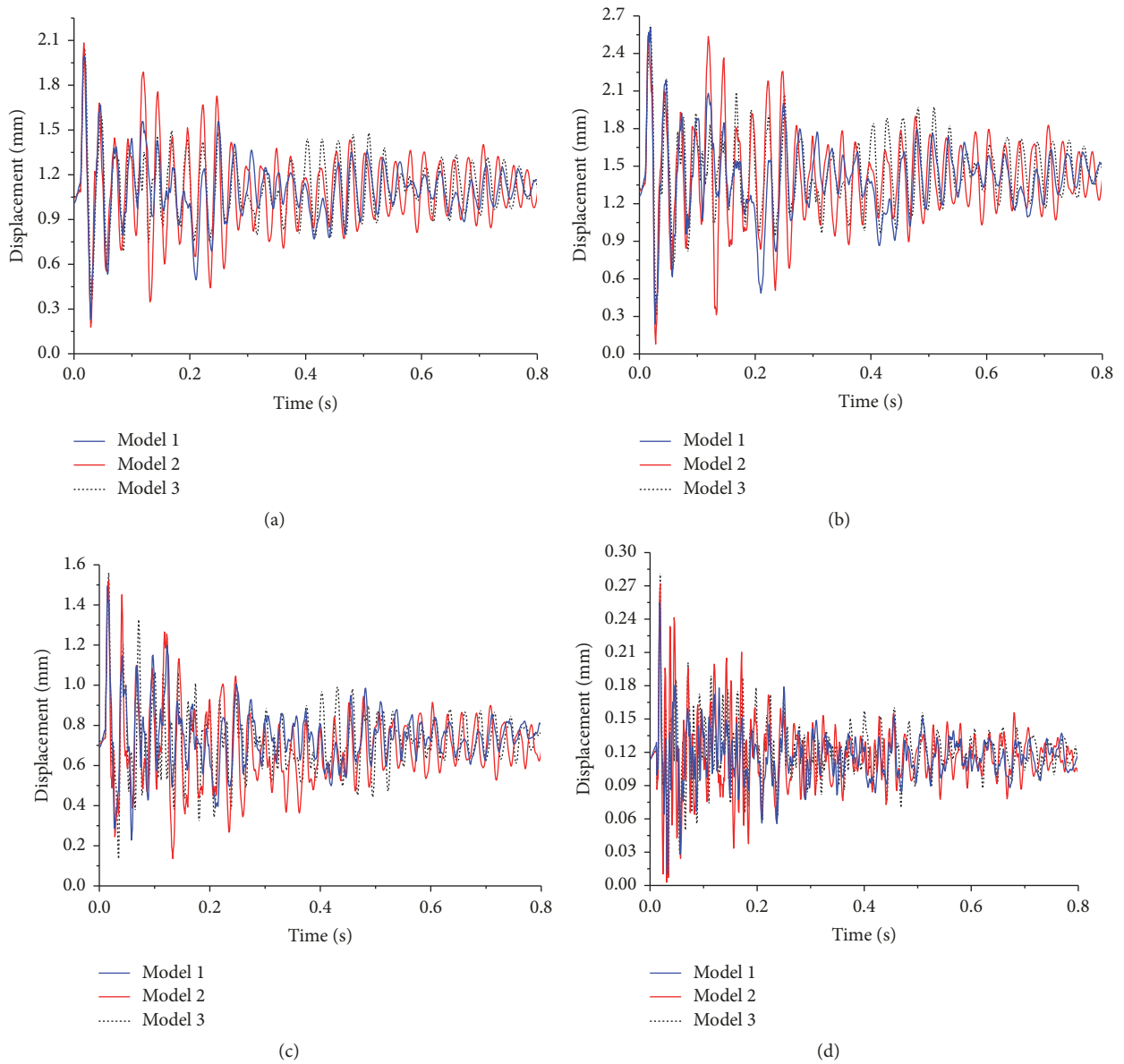


FIGURE 11: Displacement time history curve of nodes: (a) node 1, (b) node 2, (c) node 3, and (d) node 4.

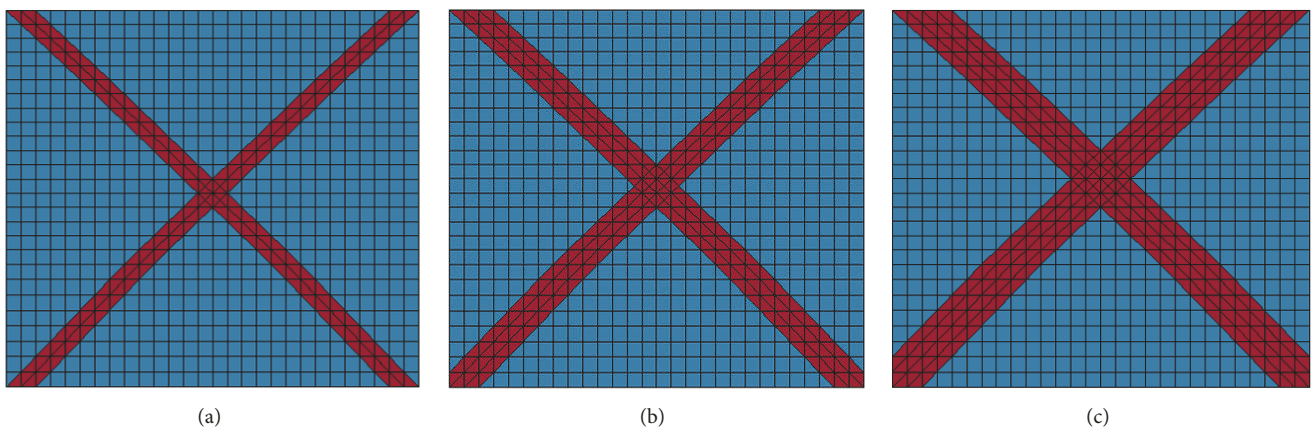


FIGURE 12: Carbon fiber layouts: (a) model 4, (b) model 5, and (c) model 6.

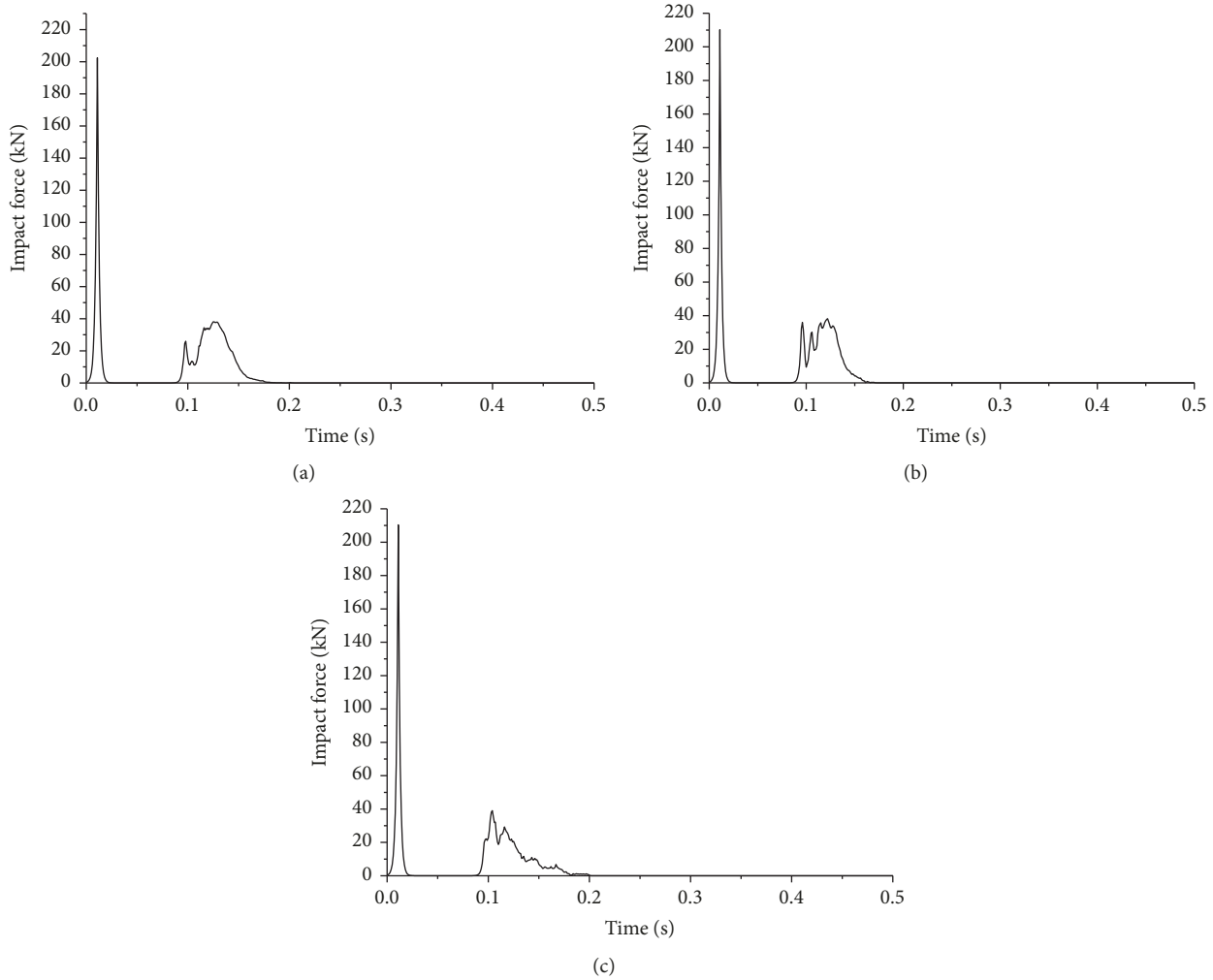


FIGURE 13: Impact time history curves: (a) model 4, (b) model 5, and (c) model 6.

the bottom of the wall. The maximum stress appears at the fixed supports connected to the ground.

By comparing the damage of the three models, model 4 yields the smallest final damage, while model 6 yields the largest. There are two main reasons for this. First, at increasing FRP widths, the duration of the interaction between the rock and FRP becomes longer. Second, the stiffness of the wall increases when the width of the carbon fiber cloth increases. According to $F = \sqrt{mv^2k}$ (where F is the impact force, m is the mass, v is the velocity, and k is the stiffness), the impact force increases with increases in stiffness. Consequently, an increased energy is absorbed by the wall when the fiber cloth is wider, which results in an increased damage.

(c) *Displacement Response.* Figure 15 shows the displacement time history curves of selected typical nodes. From these curves, the displacement patterns of the nodes in the three models are generally the same. Model 4 has the largest displacement amplitude, and the largest final residential strain, while model 6 has the smallest. This is because the deformation of the FRP cloth contributes to energy absorption, which results in decreases of the wall displacement. In

addition, the time history curve of node 4 is denser than the others, indicating that node 4 has a higher vibration frequency. As it was mentioned before, node 4 is on the structural column, whose out-of-plan stiffness is larger than that of the masonry wall. A higher stiffness leads to a higher vibration frequency.

Table 6 lists the maximum displacement of each typical node. The results from these data are consistent with the elicited results shown in Figure 15. In general, a wider fiber cloth minimizes the response of the structure after its impact by debris flow.

4.3. *Fiber Types.* To analyze the effect of different fiber types on the reinforced structure under debris flow, carbon fiber reinforced polymer (CFRP), glass fiber reinforced polymer (GFRP), and aramid fiber reinforced polymer (AFRP) were chosen. The main differences of these FRPs exist in their physical parameters, including their elastic moduli, tensile strengths, and ultimate elongation rates.

4.3.1. *Scheme of Reinforcement.* Some of the main physical parameters of the CFRP, GFRP, and AFRP are listed in

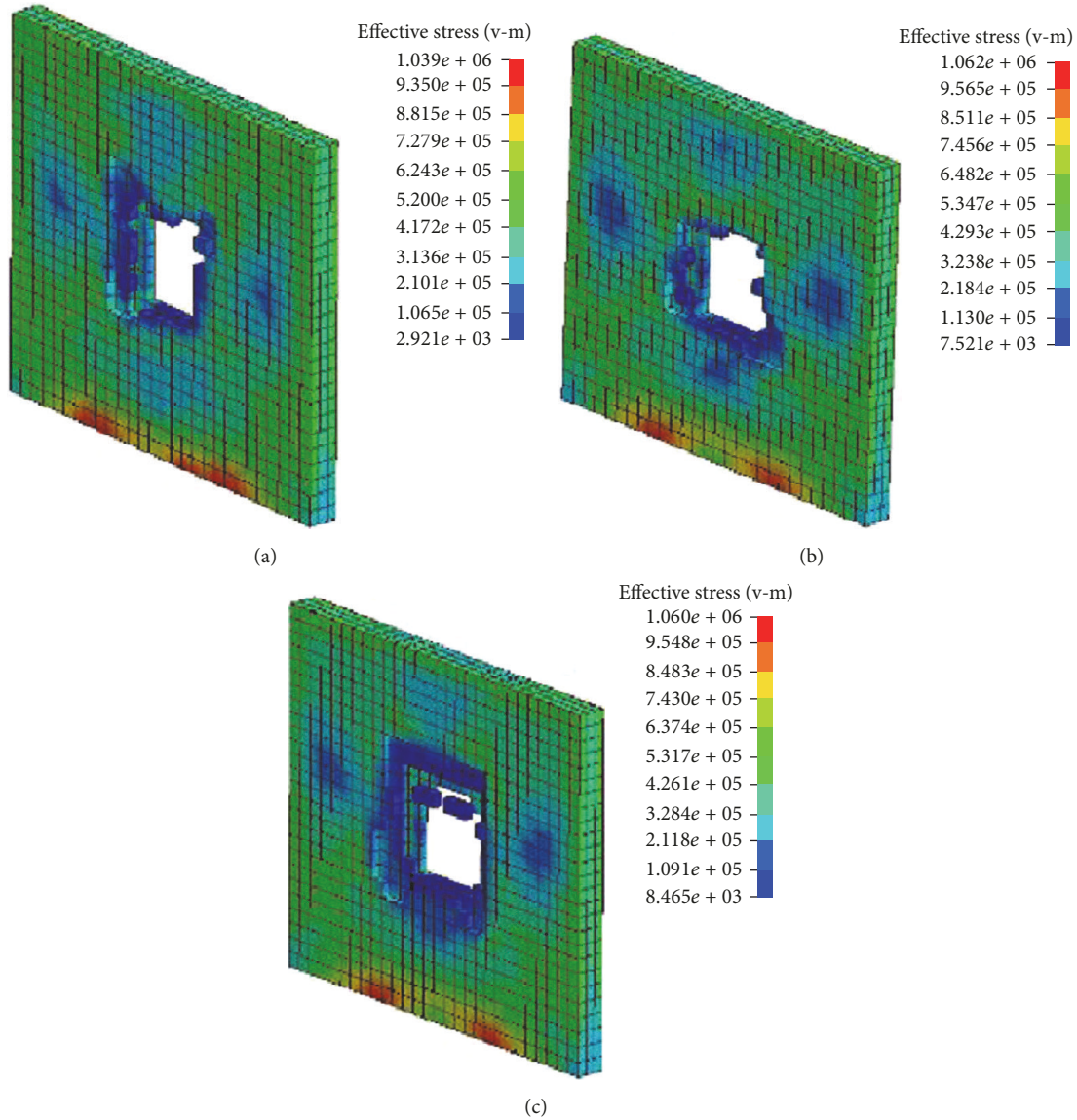


FIGURE 14: Stress contours of impacted walls at $T = 300$ ms: (a) model 4, (b) model 5, and (c) model 6.

TABLE 6: Maximum displacements (mm) elicited by the three models.

Node	Model		
	4	5	6
1	2.03	1.99	1.96
2	2.65	2.60	2.47
3	1.67	1.49	1.47
4	0.27	0.25	0.24

Table 7. It can be found that CFRP has the largest tensile and elastic modulus values, whereas GFRP has the largest density and AFRP the largest ultimate elongation rate. The adopted scheme of reinforcement is shown in Table 8.

4.3.2. Dynamic Response

(a) *Rock Impact Time History Curves.* Figure 16 shows the impact time history curves for models 7 to 9. It can be seen that the peak values of the impact force of models 7 to 9 are 221 kN, 219 kN, and 213 kN, respectively. The magnitude of the impact forces and the duration of the interactions exhibit minor differences in these models. This is primarily owing to the different elastic moduli of the three FRP materials. Furthermore, as previously mentioned, the generated irregular patterns of the curves after the rock penetrates the wall are complex, and this is an outcome of the induced vibration owing to the specific model.

(b) *Damage Response.* Figure 17 shows the stress contours of models 7 to 9 at $T = 300$ ms. It can be seen that the local damage is the main failure mode of the walls. In

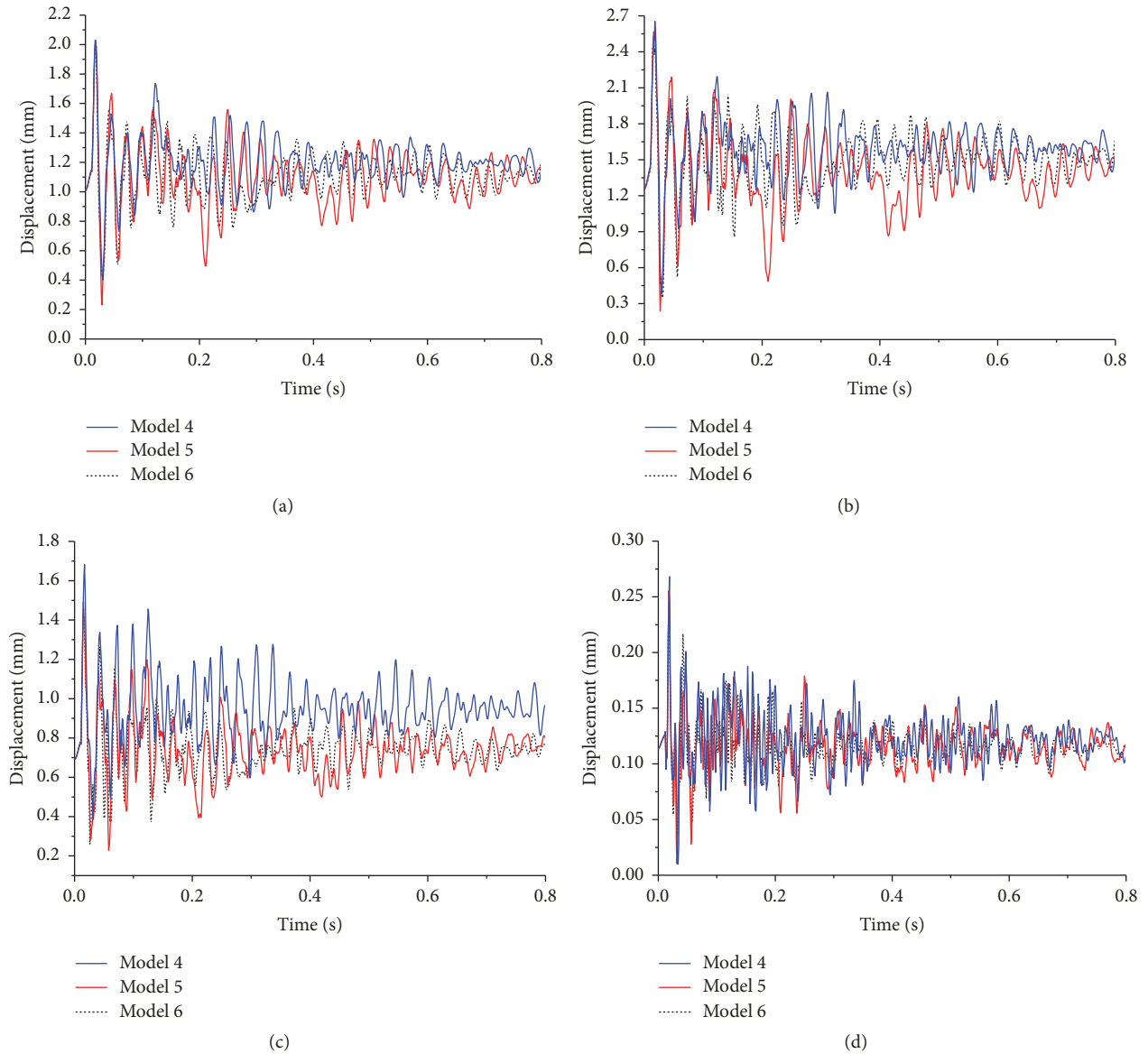


FIGURE 15: Node displacement-time curve: (a) node 1, (b) node 2, (c) node 3, and (d) node 4.

TABLE 7: Main physical parameters of CFRP, GFRP, and AFRP.

FRP	Density (g/cm^3)	Tensile strength (MPa)	Elastic modulus (GPa)	Ultimate elongation rate (%)
CFRP	1.8	3500	230	1.5
GFRP	2.5	3100	72.5	2.7
AFRP	1.45	2900	125	2.8

TABLE 8: Adopted scheme of reinforcement for different FRP types.

Model number	FRP	Width (mm)	Thickness (mm)	Arrangement type
7	Carbon fiber reinforced polymer (CFRP)	200	0.170	Diagonal
8	Glass fiber reinforced polymer (GFRP)	200	0.170	Diagonal
9	Aramid fiber reinforced polymer (AFRP)	200	0.170	Diagonal

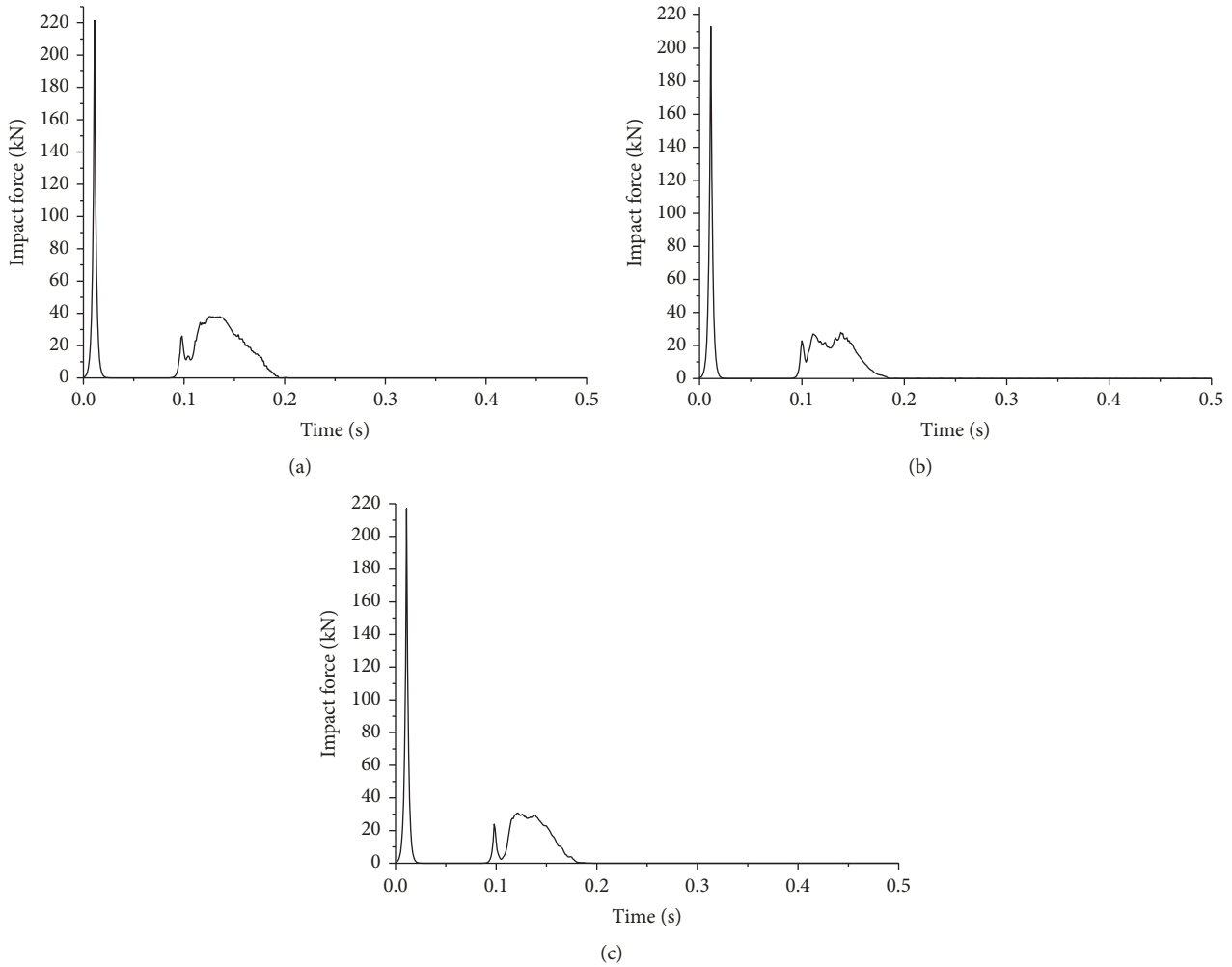


FIGURE 16: Impact time history curve: (a) model 7, (b) model 8, and (c) model 9.

addition, a certain degree of stress concentration occurs at the four corners of the hole and at the bottom of the wall. By comparing the damage of these three models, model 8 yields the smallest final damage, while model 7 yields the most severe final damage. This finding possibly relates to the elastic modulus of the FRP. As it is shown in Tables 7 and 8, model 7 is reinforced by GFRP whose elastic modulus is 72.5 GPa, and model 8 is reinforced by CFRP whose elastic modulus is 230 GPa.

(c) *Stress–Strain Response.* Figure 18 shows the stress fields for models 7 to 9 when the velocity of the rock is reduced to zero upon impact. Figure 19 shows the strain of each model at the same instant in time. At that moment, the fiber stress and strain reach their maximum values. It can be seen that the stress values of the elements around the impact position also reach the value of the largest stress. The maximum stresses of models 7 to 9 are 290 MPa, 180 MPa, and 230 MPa, respectively. These values are much smaller than the tensile strengths of the fibers. The magnitude distribution pattern of the strain is coincident with that of stress. The maximum strain values of models 7 to 9 are 0.005, 0.012, and 0.009, respectively, which are also smaller than the FRPs' ultimate

strain. The conclusion that can be inferred is that increased energy is absorbed by the fiber, and increased fiber stress is developed when the elastic modulus is increased.

(d) *Displacement Response.* Figure 20 shows the displacement time history curves of selected typical nodes. From these curves, the displacement patterns of the nodes in three models are generally the same. Model 8 yields the largest displacement amplitude, and the largest final residual strain, while model 7 yields the smallest displacement amplitude and final residual strain. Because model 8 is reinforced by CFRP with a larger elastic modulus, it can absorb more energy upon deformation, resulting in the reduction of the displacement of the entire model. In addition, the time history curve of node 4 is also denser than the others, which means that node 4 has a higher vibration frequency. As it was mentioned before, node 4 attains a higher stiffness than other nodes.

Table 9 lists the maximum displacement of each typical node. The results from these data are consistent with the results presented in Figure 20. In general, CFRP performs better under debris flow, because of its high elastic modulus.

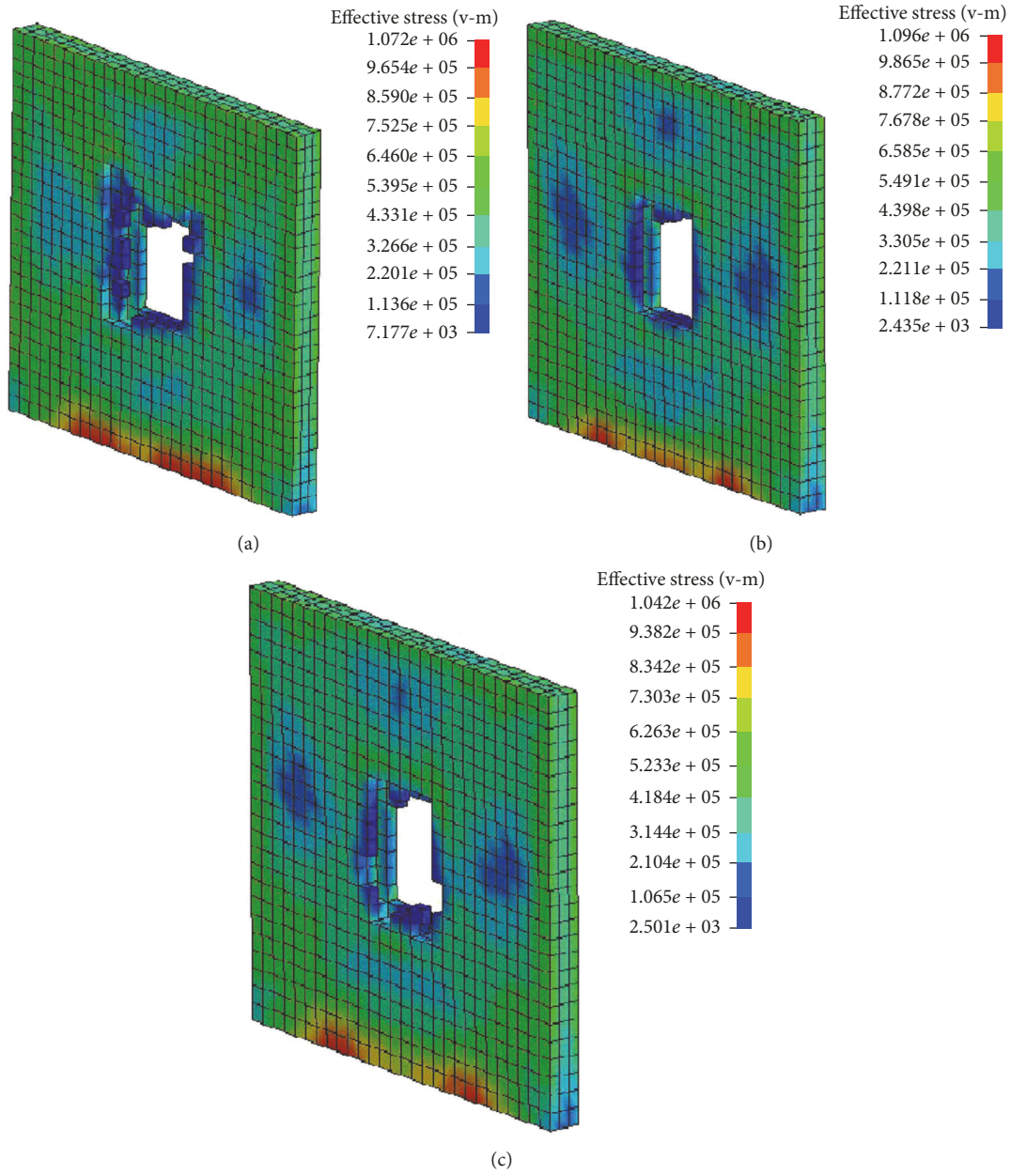


FIGURE 17: Stress contours of impacted wall at $T = 300$ ms: (a) model 7, (b) model 8, and (c) model 9.

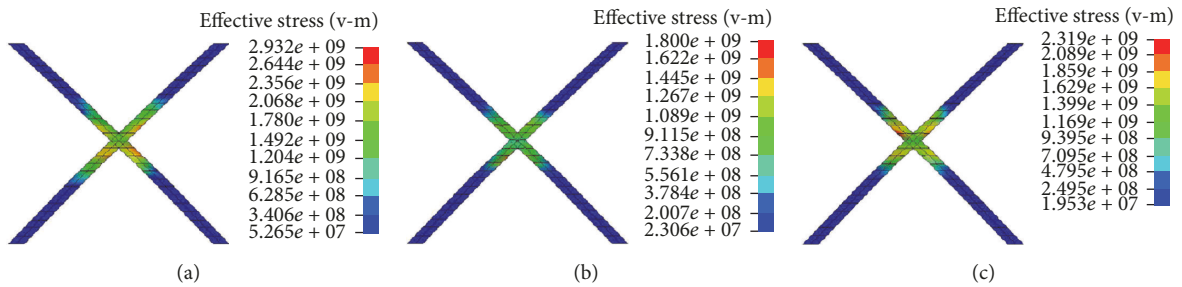


FIGURE 18: Stress contours of three models: (a) model 7, (b) model 8, and (c) model 9.

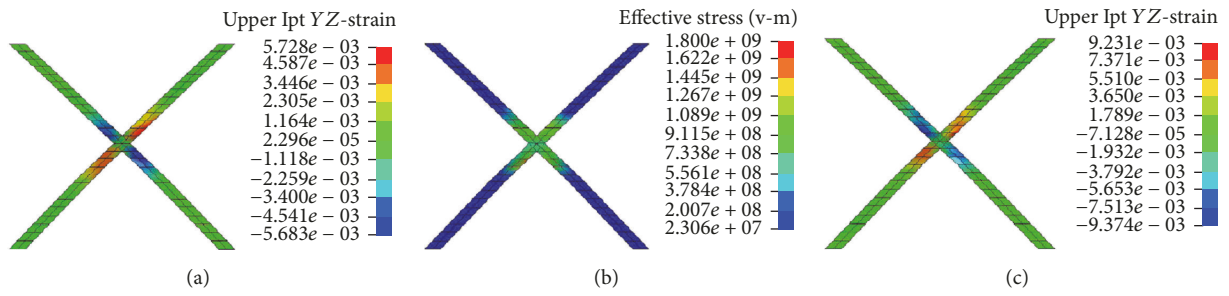


FIGURE 19: Strain contours of the three models: (a) model 7, (b) model 8, and (c) model 9.

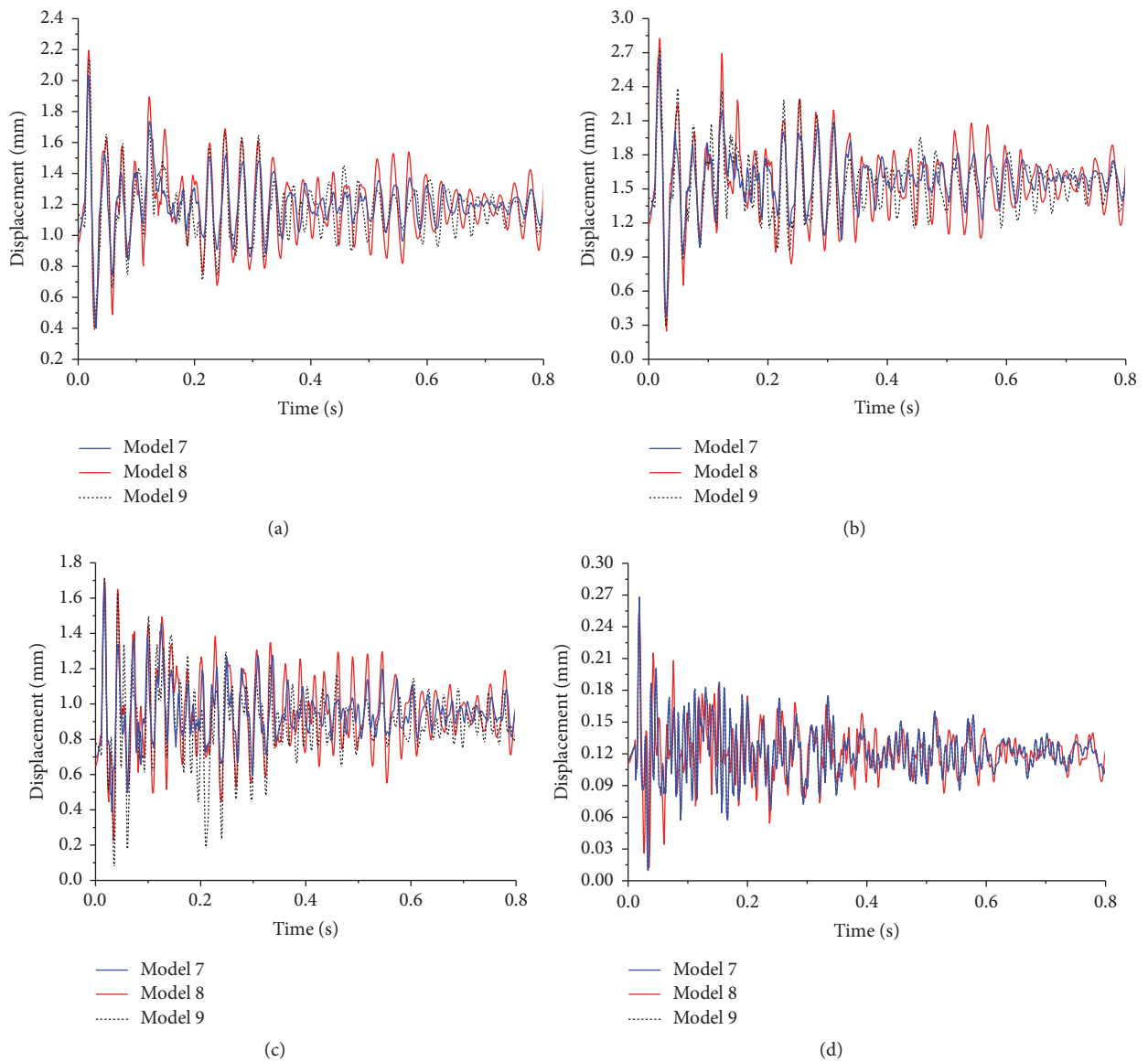


FIGURE 20: Node displacement-time curve: (a) node 1, (b) node 2, (c) node 3, and (d) node 4.

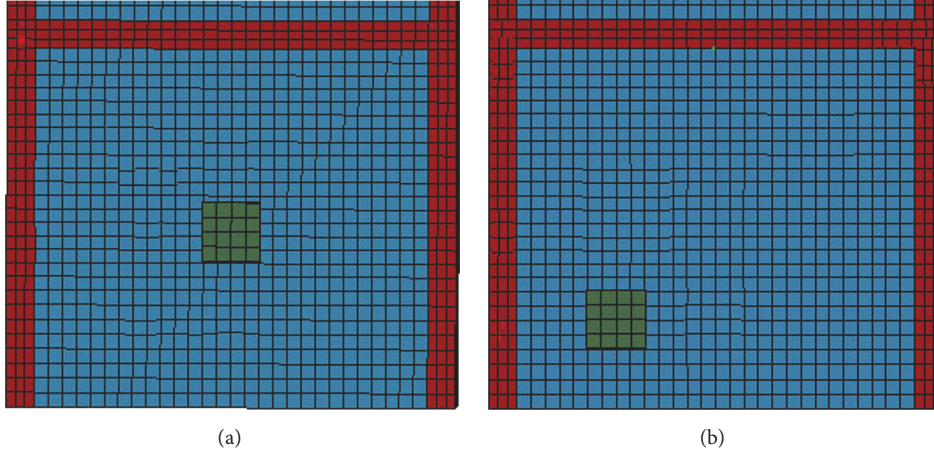


FIGURE 21: Relative impact positions: (a) model 10 and (b) model 11.

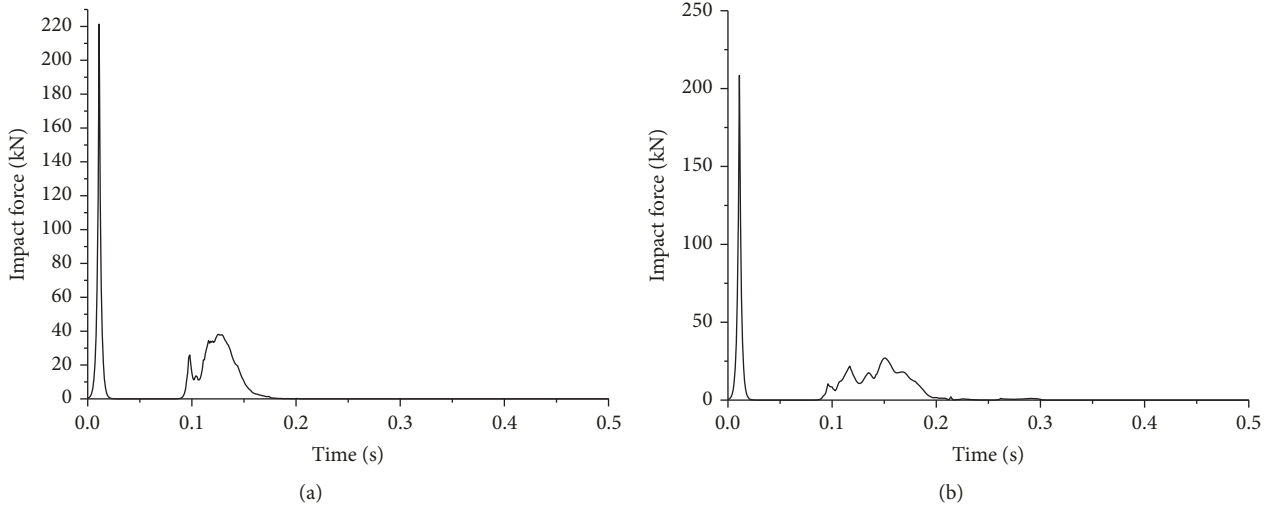


FIGURE 22: Impact time history curves: (a) model 10 and (b) model 11.

TABLE 9: Maximum displacements (mm) elicited by the three models.

Node	Model		
	7	8	9
1	2.03	2.14	2.20
2	2.62	2.83	2.74
3	1.68	1.78	1.71
4	0.26	0.27	0.27

4.4. Relative Impact Position

4.4.1. Scheme of Reinforcement. To analyze the effect of different impact positions, two models were established. As shown in Figure 3, a diagonal FRP arrangement is adopted. The widths of the FRP of the two models are 150 mm, and the thickness values are 0.167 mm. The reinforcement scheme is shown in Table 10. Figure 21 shows the relative impact positions of the two models.

TABLE 10: Scheme of reinforcement at different impact positions.

Number	Distance from the center of the impact to the bottom (mm)	Distance from the center of the impact to axis A (mm)
10	1530	1680
11	710	960

4.4.2. Dynamic Response

(a) Rock Impact Time History Curves. Figure 22 shows the impact time history curves for models 10 to 11. It can be seen that the peak values of the impact force of models 10 and 11 are 218 kN and 209 kN, respectively. This difference results from the different stiffness. The stiffness of the wall is a little larger at the center, because the area of the FRP at the cross-position is larger than that of other parts. Furthermore, as mentioned above, irregular curve patterns are elicited after the rock penetrates the wall owing to the model vibrations.

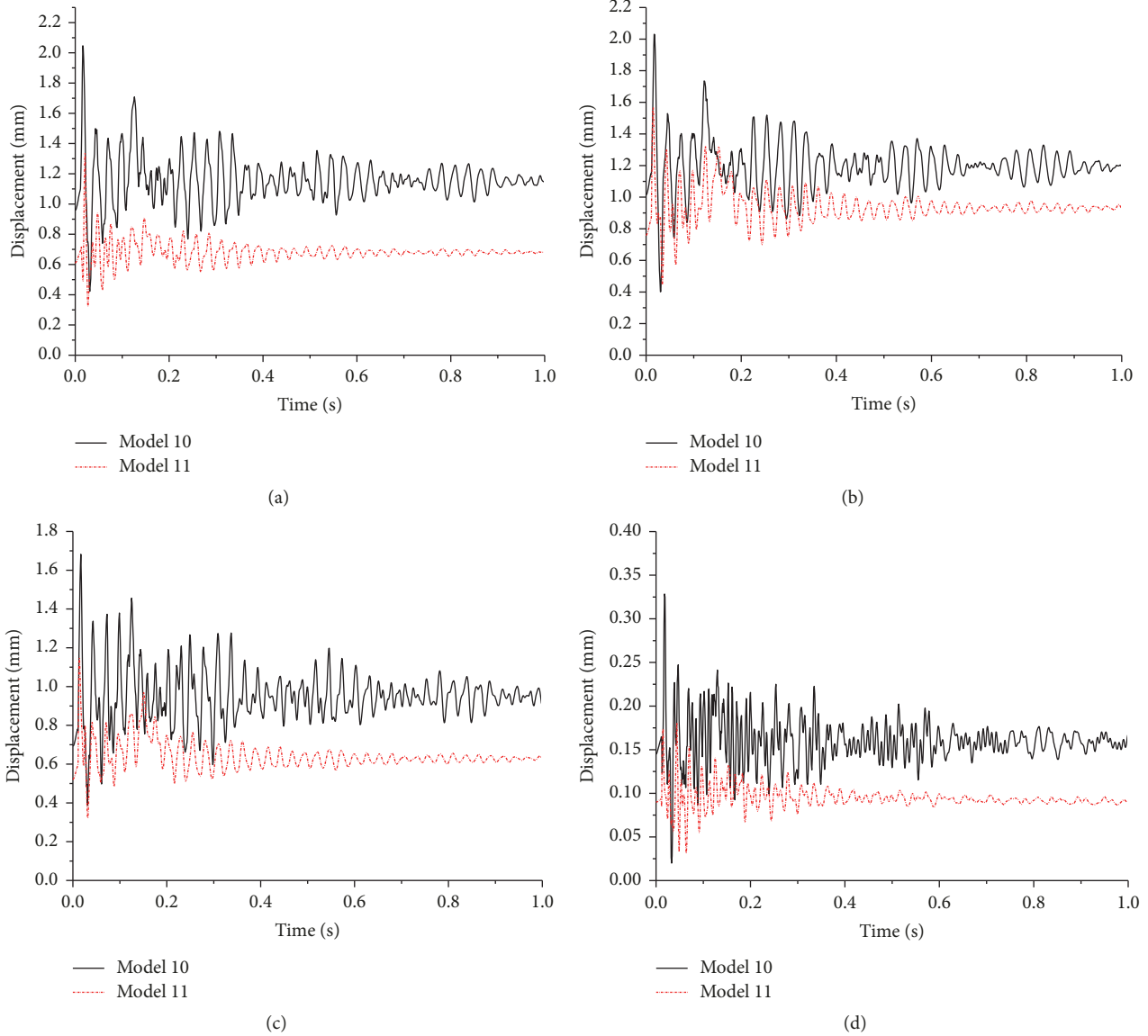


FIGURE 23: Node displacement-time curve: (a) node 1, (b) node 2, (c) node 3, and (d) node 4.

(b) *Displacement Response.* Figure 23 shows the displacement time history curves of four typical nodes. As seen, the displacement patterns of the nodes in the two models are generally the same. However, the value of the displacement in model 11 is much smaller than that of model 10. This is because the impact position of model 11 is close to the foundation of the structure. In terms of mechanics, for the forces that have the same value, the force that is closer to the anchorage end causes a smaller displacement. Table 11 lists the maximum displacements for each of the studied nodes. The results from these data are consistent with the results plotted in Figure 23.

(c) *FRP Response.* Figure 24 shows the stress distribution of FRP for the two models when maximum stress occurs. It can be seen that the maximum stress concentrates at the impact position. The maximum stress of FRP in model 10 is 293 GPa

TABLE 11: Maximum displacements (mm) elicited by the two models.

Node	Model	
	10	11
1	2.03	1.34
2	2.02	1.57
3	1.58	1.16
4	0.32	0.18

when $T = 130$ ms, while its corresponding value is 340 GPa in model 11 when $T = 150$ ms. This is because the impact is burdened by two FRP strips in model 10, but by one FRP strip in model 11. Figure 25 shows the stress time history curves of the maximum stress element in the two models. Based on the curves, it can be concluded that FRP is in the elastic stage of its

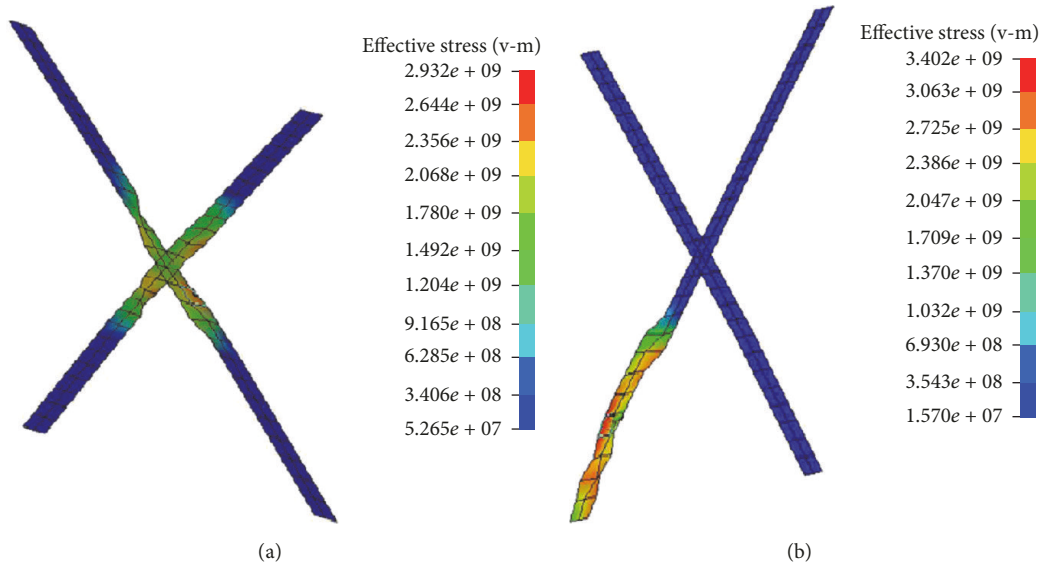


FIGURE 24: Stress distribution of FRP: (a) model 10, $T = 130$ ms, and (b) model 11, $T = 150$ ms.

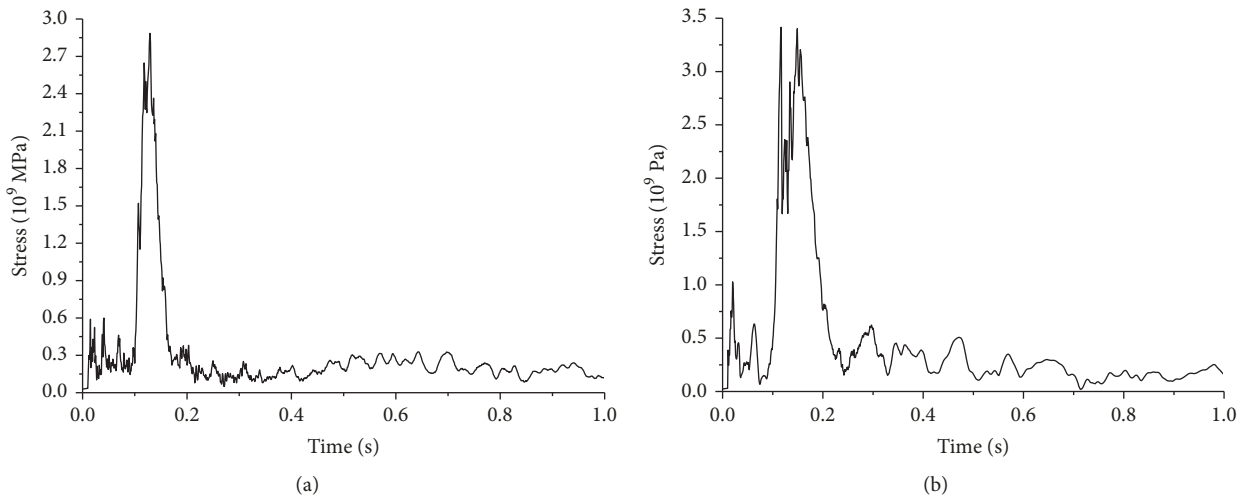


FIGURE 25: Stress time history curves of the maximum stress element in the two models: (a) model 10 and (b) model 11.

deformation during the impact. The strain is calculated to be more than 0.0002, which is far lower than the ultimate tensile strain. Accordingly, FRP is not exposed to tensile failure. In other words, the assumption that FRP is elastic is proven.

In general, it can be concluded that the impact at the center is more unfavorable than at the corner. Consequently, it is reasonable to simulate the constructed models using an impact position set at the center of the wall.

5. Application Proposals

Based on the detailed parametric study and the discussion on the corresponding mechanism introduced in Section 4, some suggestions of engineering applications in debris flow hazard areas can be proposed:

(1) For FRP-reinforced masonry structures, the dynamic performance under debris flow varies based on different FRP

arrangements and FRP material types. The importance of these differences should be reflected in the design codes in the future. However, further studies should be carried out to determine the details of these parameters.

(2) The width of FRP is an essential parameter for reinforcing masonry structures. If civil engineers need to control local damage, narrower widths of FRPs are favorable, but wider FRP widths are more suitable in controlling the overall displacement. However, the achievement of a consistent one-to-one match between values of the FRP width and the degrees of local damage, or the overall displacements, requires further studies.

(3) Although there is a reinforcement code in China, FRP reinforcement regulations for masonry structures under debris flow cannot be referred. These regulations, such as the ones pertaining to failure criteria, demand more in-depth studies. Suggestions on the failure criteria can be determined

by the destruction of walls, failure of FRP, or by surpassing the limitation of the overall displacement.

6. Conclusion

In this study, the influences of different parameters on the dynamic response of FRP-reinforced masonry structures under viscous debris flow are discussed. Because the application of FRP in resisting debris flow has been seldomly studied before, this study is valuable and necessary for its further application in masonry structures in resisting debris flow. The following conclusions are obtained based on parametric studies by analyzing the numerical simulation results:

(1) The reinforced model performed better than the unreinforced model under debris flow. The parametric study on the dynamic response of FRP-reinforced masonry structures under debris flow impacts was necessary.

(2) The arrangement of reinforced FRP was an important parameter that influenced responses of masonry structures under debris flow. Generally, the diagonal and the intersecting parallel types of FRP arrangements yielded better performances than the horizontal type. The carbon fibers arranged in diagonal and intersecting parallel arrangements induced a more uniform wall stress distribution. Additionally, different arrangements also led to different shapes of local damage of masonry walls.

(3) The widths of the reinforced FRP materials had a profound influence on the structural behavior. A wider fiber cloth led to a minimized structural response impacted by debris flow, and resulted in more severe local damage.

(4) The elastic modulus was the dominant physical parameter that influenced the dynamic response of the masonry structure reinforced by different types of FRP. GFRP yielded the smallest elastic modulus value among all the three types and had the most significant effect in reducing the local damage, while the CFRP yielded a better structural response under debris flow because of its high elastic modulus, which ultimately helped the fiber absorb more energy.

(5) The impact at the center was more unfavorable than that at the corner. Consequently, it was reasonable to conduct a parametric study on the dynamic response of FRP-reinforced masonry structures with the debris impact at the center of the wall.

Conflicts of Interest

The authors declare that they have no conflicts of interest.

Acknowledgments

The financial support that was received from the National Key Technology R&D Program through Grant 2014BAL05B01 is highly appreciated.

References

- [1] X. Tang, *Debris Flows in China*, The Commercial Press, Beijing, China, 2000.
- [2] B.-H. Jun, "Numerical simulation of the topographical change in Korea mountain area by intense rainfall and consequential debris flow," *Advances in Meteorology*, vol. 2016, Article ID 9363675, 11 pages, 2016.
- [3] W. Zhang, Q. Wang, J. Chen, H. Li, J. Que, and Y. Kong, "Grain-size analysis of debris flow alluvial fans in Panxi Area along Jinsha River, China," *Sustainability*, vol. 7, no. 11, pp. 15219–15242, 2015.
- [4] F. Tang, "Finite element analysis of seismic resistance of masonry structure in rural China," *Advanced Materials Research*, vol. 827, pp. 328–333, 2014.
- [5] Z. Lu, Y. Yang, X. Lu, and C. Liu, "Preliminary study on the damping effect of a lateral damping buffer under a debris flow load," *Applied Sciences*, vol. 7, no. 2, article no. 201, 2017.
- [6] S. Q. Yang, "Introduction of National Comprehensive Disaster Prevention and Reduction Plan," *Disaster Reduction in China*, no. 1, pp. 20–22, 2017.
- [7] Z. Lu, D. Wang, S. F. Masri, and X. Lu, "An experimental study of vibration control of wind-excited high-rise buildings using particle tuned mass dampers," *Smart Structures and Systems*, vol. 18, no. 1, pp. 93–115, 2016.
- [8] Z. Lu, X. Chen, D. Zhang, and K. Dai, "Experimental and analytical study on the performance of particle tuned mass dampers under seismic excitation," *Earthquake Engineering & Structural Dynamics*, vol. 46, no. 5, pp. 697–714, 2017.
- [9] Z. Lu, X. Lu, H. Jiang, and S. F. Masri, "Discrete element method simulation and experimental validation of particle damper system," *Engineering Computations*, vol. 31, no. 4, pp. 810–823, 2014.
- [10] K. Dai, J. Wang, R. Mao, Z. Lu, and S.-E. Chen, "Experimental investigation on dynamic characterization and seismic control performance of a TLPD system," *The Structural Design of Tall and Special Buildings*, vol. 26, no. 7, Article ID e1350, 2017.
- [11] Z. Lu, X. Chen, X. Lu, and Z. Yang, "Shaking table test and numerical simulation of an RC frame-core tube structure for earthquake-induced collapse," *Earthquake Engineering & Structural Dynamics*, vol. 45, no. 9, pp. 1537–1556, 2016.
- [12] Z. Lu, Z. Wang, S. F. Masri, and X. Lu, "Particle impact dampers: Past, present, and future," *Structural Control and Health Monitoring*, vol. 25, no. 1, article e2058, 2018.
- [13] Z. Lu, X. Chen, and Y. Zhou, "An equivalent method for optimization of particle tuned mass damper based on experimental parametric study," *Journal of Sound and Vibration*, 2017.
- [14] Z. Lu, B. Huang, and Y. Zhou, "Theoretical study and experimental validation on the energy dissipation mechanism of particle dampers," *Structural Control and Health Monitoring*, 2017.
- [15] J. Wu, *Debris-Flow and Comprehensive Management*, Science Press, Beijing, China, 1993.
- [16] G. Kuwabara and K. Kono, "Restitution coefficient in a collision between two spheres," *Japanese Journal of Applied Physics*, vol. 26, no. 8R, pp. 1230–1233, 1987.
- [17] American Association of State Highways and Transportation Officials, "LRFD bridge design specifications," Washington, DC, USA, 1998.
- [18] O. Hungr, G. C. Morgan, and R. Kellerhals, "Quantitative analysis of debris torrent hazards for design of remedial measures," *Canadian Geotechnical Journal*, vol. 21, no. 4, pp. 663–677, 1984.
- [19] J. Xie, *Study on the new technique of repairing and strengthening masonry walls with continuous carbon fiber sheet*, Doctor's Thesis, Tianjin University, Tianji, China, 2005.

- [20] G. Schwegler, "Masonry construction strengthened with fiber composites in seismically endangered zones," in *Proceedings of the 10th European Conference on Earthquake Engineering*, vol. 3, pp. 2299–2303, Vienna, Austria, 1994.
- [21] F. Seible, "Repair and seismic retest of a full-scale reinforced masonry building," in *Proceedings of the 6th International Conference on Structural Faults and Repair*, vol. 3, pp. 229–236, Edinburgh, UK, 1995.
- [22] X. Wang, Z. Lu, and X. Lu, "An investigation of the aseismic behavior of masonry structures strengthened by carbon fiber reinforced plastics," *Industrial Construction*, vol. 33, no. 9, pp. 11–13, 2003.
- [23] D. Laigle, P. Lachamp, and M. Naaim, "SPH-based numerical investigation of mudflow and other complex fluid flow interactions with structures," *Computational Geosciences*, vol. 11, no. 4, pp. 297–306, 2007.
- [24] C. Zeng, P. Cui, and Y. Ge, "Characteristic and mechanism of buildings damaged by debris flows on 11 July, 2013 in Qipangou of Wenchuan, Sichuan," *Journal Earth Science and Environment*, vol. 36, no. 2, pp. 81–91, 2014.
- [25] Y. Guo, Z. Yu, and L. Guo, "Impacting testing methods for masonry wall based on the drop hammer," *Structural Engineering*, vol. 28, no. 6, pp. 123–127, 2012.
- [26] P. Li, T. Li, Z. Lu, and J. Li, "Study on dynamic response of novel masonry structures impacted by debris flow," *Sustainability*, vol. 9, no. 7, article no. 1122, 2017.
- [27] T.-L. Teng, C.-C. Liang, and T.-T. Tran, "Development and validation of a finite element model for road safety barrier impact tests," *Simulation-Transactions of the Society for Modeling and Simulation International*, vol. 92, no. 6, pp. 565–578, 2016.
- [28] O. I. Abdelkarim and M. A. ElGawady, "Dynamic and static behavior of hollow-core FRP-concrete-steel and reinforced concrete bridge columns under vehicle collision," *Polymer*, vol. 8, no. 12, article no. 432, 2016.
- [29] C. Reuter, K.-H. Sauerland, and T. Tröster, "Experimental and numerical crushing analysis of circular CFRP tubes under axial impact loading," *Composite Structures*, vol. 174, pp. 33–44, 2017.
- [30] G. S. Chandekar and A. D. Kelkar, "Experimental and numerical investigations of textile hybrid composites subjected to low velocity impact loadings," *The Scientific World Journal*, vol. 2014, Article ID 325783, 14 pages, 2014.
- [31] X. Wei and M. G. Stewart, "Model validation and parametric study on the blast response of unreinforced brick masonry walls," *International Journal of Impact Engineering*, vol. 37, no. 11, pp. 1150–1159, 2010.
- [32] H. M. Elsanadedy, T. H. Almusallam, S. H. Alsayed, and Y. A. AL-Salloum, "Experimental and FE study on RC one-way slabs upgraded with FRP composites," *KSCE Journal of Civil Engineering*, vol. 19, no. 4, pp. 1024–1040, 2015.
- [33] D. Proske, J. Suda, and J. Hubl, "Debris flow impact estimation for breakers," *Georisk Assessment & Management of Risk for Engineered Systems & Geohazards*, vol. 5, no. 2, pp. 143–155, 2011.
- [34] N. He, N. S. Chen, and C. Zeng, "Current situation and tendencies of debris flow initiation mechanism," *Journal of Catastrophology*, vol. 28, no. 1, pp. 121–125, 2013.
- [35] C. Zeng, P. Cui, Z. Su, Y. Lei, and R. Chen, "Failure modes of reinforced concrete columns of buildings under debris flow impact," *Landslides*, vol. 12, no. 3, pp. 561–571, 2015.
- [36] *Ministry of Housing and Urban-Rural Construction of the People's Republic of China. Code for design of masonry structures GB 5003-2011*, China Architecture & Building Press, Beijing, China, 2011.
- [37] S. Zhang, D. Yang, Y. Sheng, S. W. Garrity, and L. Xu, "Numerical modelling of FRP-reinforced masonry walls under in-plane seismic loading," *Construction and Building Materials*, vol. 134, no. Supplement C, pp. 649–663, 2017.
- [38] G. Wang, *Debris flow impact pressure signal processing by the wavelet analysis, Doctoral Thesis*, University of Science and Technology of China, Hefei, China, April 2017.
- [39] P. Li, J. Li, and T. Li, "The failure mechanism of masonry structure under debris flow impact," *Journal of Huazhong University of Science and Technology (Natural Science Edition)*, vol. 45, no. 7, p. 1-5+29, 2017.
- [40] S. Govindjee, G. J. Kay, and J. C. Simo, "Anisotropic modelling and numerical simulation of brittle damage in concrete," *International Journal for Numerical Methods in Engineering*, vol. 38, no. 21, pp. 3611–3633, 1995.
- [41] "LS-DYNA Theoretical Manual," Livermore Software Technology Corporation, May 2007, http://ftp.lstc.com/anonymous/outgoing/jday/manuals/ls-dyna.971_manual_k_rev1.pdf.
- [42] S.-L. Xu and Q. Fang, "Numerical analysis on blast-resistant capacity of masonry walls retrofitted with elastomeric polymer and CFRP," *Journal of PLA University of Science and Technology (Natural Science Edition)*, vol. 11, no. 3, pp. 306–311, 2010.
- [43] Y. R. Guo and H. Zheng, "Numerical simulation of CFRP strengthened perforated masonry walls under blast loading," *Advanced Materials Research*, vol. 640, no. 1, pp. 727–731, 2012.
- [44] J. B. Tang, K. H. Hu, G. D. Zhou, H. Y. Chen, X. H. Zhu, and C. Ma, "Debris flow impact pressure signal processing by the wavelet analysis," *Journal of Sichuan University (Engineering Science Edition)*, vol. 45, pp. 8–13, 2013.



Hindawi

Submit your manuscripts at
www.hindawi.com

